IEEE Access
Multidisciplinary | Rapid Review | Open Access Journal

Received 27 July 2024, accepted 22 September 2024, date of publication 27 September 2024, date of current version 29 October 2024.

Digital Object Identifier 10.1109/ACCESS.2024.3469791

RESEARCH ARTICLE

Vibration Characteristics Analysis of Elderly-Robot Couple System for Transporting Posture of Elderly-Assistant Robot

KHALED HAMZA[1,2], ZHANG XIAODONG[1,3], MU XIAOQI[1,3], GILBERT MASENGO[1], AND AHMAD BALA ALHASSAN[4], (Member, IEEE)

[1]School of Mechanical Engineering, Xi'an Jiaotong University, Xi'an, Shaanxi 710049, China
[2]Faculty of Engineering at Benha, Benha University, Benha 13511, Egypt
[3]Shaanxi Key Laboratory of Intelligent Robot, Xi'an Jiaotong University, Xi'an 710049, China
[4]Department of Robotics and Mechatronics, School of Engineering and Digital Sciences, Nazarbayev University, 010000 Astana, Kazakhstan

Corresponding author: Khaled Hamza (khaledhamza@stu.xjtu.edu.cn)

This work was supported in part by the Qin Chuang Yuan "Scientist + Engineer" Team Construction Project of Shaanxi Province under Grant 2022KXJ-160, and in part by the Fundamental Research Funds for the Central Universities under Grant xhj032021009-06.

ABSTRACT With the growing elderly population worldwide, it is crucial to develop an advanced elderly-assistant robot that can assist healthcare workers and reduce the care burden on society. Nonetheless, older people, often associated with decreased muscle strength and increased fatness, could be adversely affected by the induced vibration of the assistant robots. Thus, to help older people execute daily activities while reducing vibration impacts, the vibration characteristics analysis of the human-robot coupled system for the transporting posture of the elderly-assistant robot (EAR) is presented in this paper. The equations of motion for the coupled elderly-EAR system are established using Newton's second law. Then, the dynamic behavior of the model is investigated and analyzed in a Matlab simulation environment for different road roughness and robot speeds. In addition, real-time experimental analysis was conducted to verify the effectiveness of the derived model using asphalt and interlock roads for the EAR's speeds of 4.5km/h and 7km/h. The simulation and the experimental results show that the derived model can be efficiently applied to assess the robot-user vibration transmissibility of the road-induced vibration. Finally, the ISO 2631-1 based comfortability analysis demonstrates guaranteed EAR's stability and ride comfort of the elders on asphalt and interlock roads.

INDEX TERMS Vibration analysis, dynamic model, EAR, ride comfort, elder-robot couple model.

I. INTRODUCTION

The elderly who are 60 and older are the world's fastest-growing population group. However, their physical activities are reduced due to aging, often characterized by decreased muscle strength and increased fatness. Generally, when people reach the age of fifty, their muscles' mass and strength steadily decline in a process called sarcopenia. This muscle declination leads to the poor physical strength of older people and hence reduced independence [1], [2].

According to the United Nations' 2020 Population Aging Report [3], it projects that by the year 2050, the population of older people would increase to 21.4% of the global population from 13.2% in 2019, 11.7% in 2013, 9.88% in 2000 and 8% in 1950. Also, according to the WHO's 2011 World Report on Disability [4], 20% of the global population (5.1% less than 14 years old and 14.9% between 15 and 59 years old) have a moderate and severe impairment. This demonstrates that the percentage of people needing a special assistant to execute

The associate editor coordinating the review of this manuscript and approving it for publication was Jason Gu.

daily activities will significantly increase, leading to higher pressure on the healthcare system and a substantial economic burden on society.

Thus, developing an advanced elderly-assistant robot is crucial to assisting healthcare workers and reducing the care burden on families and society. Ward et al. [5] assess the importance of a power wheelchair for patients with Amyotrophic lateral sclerosis (ALS), a nervous system disease. The survey showed that the mobility, comfortability and life quality of the patients have considerably improved with decreased pain. Fascinatingly, many researchers have introduced various kinds of elderly-assistant mechanisms around the world to enhance the daily activities of older people [6], [7]. Some of these assistant robots have been developed and adapted for particular uses, such as home companionship robots [8], health institutions for nursing care [9], and transporting aids, which are the primary motivation of this paper.

The Elder-Assistant Robot (EAR) is a multifunctional robot that assists the elderly in walking with a smart cane and transports them as an intelligent wheelchair. As safety and comfortability are the most crucial issues for older people who use EAR or intelligent wheelchairs, most of the research on EAR has focused on improving the design and the operations of the robots for better ride comfort for the users. For instance, Park et al. [10] developed an intelligent wheelchair (ichair) that the user's head can control. The system was equipped with sensors that can measure the rotation angles of the wheelchair, the blood pressure, and other user properties and send the information as a text message to the designated caregivers for monitoring. The system serves as a monitor for the user's safety, especially for checking whether the user has fallen or not. Also, a power wheelchair that the user's eye-gaze can control is introduced [11]. The system uses an N-cell to navigate the wheelchair in an unstructured environment, and it is equipped with an emergency off switch if the user feels unsafe. To avoid falls and other hazardous incidents from inexperienced power wheelchair users, virtual training is introduced for new users of powered wheelchairs [12], [13].

Park et al. [10] used gyro and tilt sensors to decrease the falling risks of wheelchair users by controlling the seat angle. However, this method needs two motors for seat control and the motors that drive the wheelchair, which consumes a lot of power. Kundu et al. [11] introduce an electric wheelchair equipped with omnidirectional wheels and a front-wheel suspension system that minimizes wheelchair vibration. The study experimented on five users on a very smooth lane. Based on the results, the average vibration was reduced from 1.091g to 1.057g, which shows little effect on the suspension system. In [12] and [13], a model predictive control was used to increase the user's comfort and to avoid collision. However, when the optimum control sequence is computed, the wheelchair's future potential motion is unknown. As a result, the control assumed constant speed or acceleration, which is not the case.

In [14], [15], and [16], a ''comfortable map'' idea was introduced, which offers a navigation method for autonomous wheelchairs that is both secure and comfortable for wheelchair users and pedestrians. Also, anti-vibration or isolators were used [17] to minimize the vibration transmitted from the machine to the human body. However, the isolators were only used to reduce the vibration at the machine's handles. Additionally, different methods were used to attenuate vibration and increase the safety and comfortability of the user, such as using dynamic absorbers [18], [19], suspension systems [20], [21], and cushioning [22], [23], [24]. Although these methods are effective, their performance depends on the appropriate design and development of the wheelchairs.

Dynamic modeling and simulation analysis are crucial for assessing the design performance of the EAR, especially in hazardous situations where users could be at risk for the experimental test. Thus, it is essential to perform the dynamic analysis of the robot-user system before practical application of the system by the users. Some studies that used springs, dampers, and masses to represent the human-seat couple system were presented [25], [26], [27]. Also, Matsuoka proposed a model for a vehicle equipped with wheelchair transporting apparatus (WTA) [28], [29], [30]. In the study, the wheelchair user was described as having five rigid masses linked by rotational dampers and springs, while a single rigid mass was used for the wheelchair. Here, the induced vibrations of the wheelchair can cause the user to feel uncomfortable. Other researchers [31], [32], [33], [34], [35], [36] have used the concept of an inverted pendulum to model the user, whereby the torsional springs and dampers represent the user's muscles. Also, the backrest's impedance was represented by the stiffness and damping in the backrest. These studies examined the relationship between the riding comfort and safety of the users.

Another model of a wheelchair user subjected to vibration is described [37]. The study modeled the system into transitional and rotational sections. The user's lower torso and the seat cushion are represented as the rigid transitional component, while the user's upper torso is defined as the rigid rotational transitional component. The rotational springs and dampers reflected the relationship between the two elements. However, in [38] and [39], the wheelchair is modeled as a half car, whereby the head and body of the user are structured with rigid masses connected by a linear spring and damper. Also, the wheelchair was modeled as a single mass attached to the user through a linear damper and spring. Thus, to improve the EAR's ride comfort for older people, a multi-function robot was developed by the authors' lab [40], [41], [42], [43]. An electric linear actuator allows the robot to adjust its pose. When the elder wants to use the robot as a guide walking cane, the system is straightened up, and the seat holds up. If the elder uses it as a wheelchair, the seat returns to its original position, and the robot's stance is adjusted to accommodate the elder. In [44], the vibration characteristics of the EAR for the walking posture were studied without considering the transporting (seated) posture.

This research presents the results of the dynamic analysis of the elder-robot coupled system for transporting posture

under various road roughness. The equations are delivered using Newton's second law by describing each component of the robot and the user according to the mass-spring-damper concept. An in-depth analysis of the vibration transmissibility of the road-robot-user interaction is conducted to confirm the effectiveness of the robot design. MATLAB simulation software analyzes the system's vibration characteristics while the model's accuracy is verified experimentally using the laboratory EAR.

The remainder of the paper is divided into the following sections: The composition, function, and dynamic model of the EAR are presented in section II. Section III describes and analyzes the elder-robot coupled model simulation. The setup for the experiment and results analysis are presented in section IV. Section V shows the conclusion and recommendations.

II. THE EAR & ITS DYNAMIC MODEL

A. ROBOT DESCRIPTION

The structural design of the elderly-assistant and walking-assistant robot considered in this paper is illustrated in Fig. 1. As shown, the system consists of two twin herringbones, a folding mechanism for altering the robot's posture, tactile-slip sensors that serve as man-machine interfaces, and a trunk that houses the robot's control and driver circuits. Also, two linear electrical actuators were installed between the legs of the robot to allow it to switch between walking and transportation postures and vice versa. The front wheels (hub motors) drive the robot, while the speed difference between the left and right front wheels defines the robot's path. The wheels on the back are universal. The robot arm's maximum adjustable height is 1150mm, and the gap between the front and back wheels is 650mm, which can be balanced using the primary electric actuator. In the wheelchair delivery position, the arm of the robot in the lowest point is 740mm, and the seat height is around 500mm.

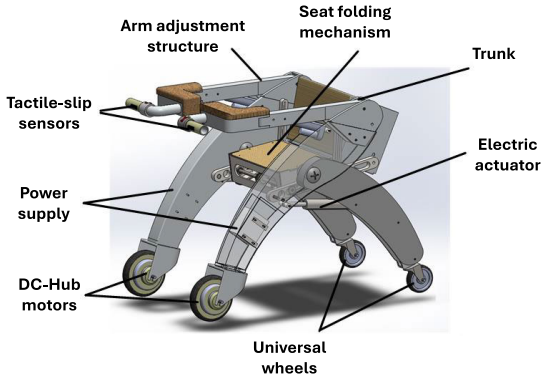

FIGURE 1. The main structure of EAR.

B. DYNAMIC MODEL

The dynamic model of the elder-robot coupled system is derived using Newton's second law, which is presented in this section. Figure 2 depicts the schematic diagram of the elder-robot system in transporting posture. The proposed model comprises six rigid masses, expressed in red, representing the elder's head, body, hands, and legs. Also, the elder muscles are defined by the springs and dampers that bind the masses. A rigid mass with linear springs and dampers was used to describe the robot, expressed in a blue line. The robot's motion is considered vertical and rotary, while the elder's motion is considered only to move vertically.

The following are the basic simplifying assumptions made for the dynamic modeling:

- The rigid object idealizes a solid body that ignores deformation.
- The dampers and springs handle all the rigid objects' interactions.

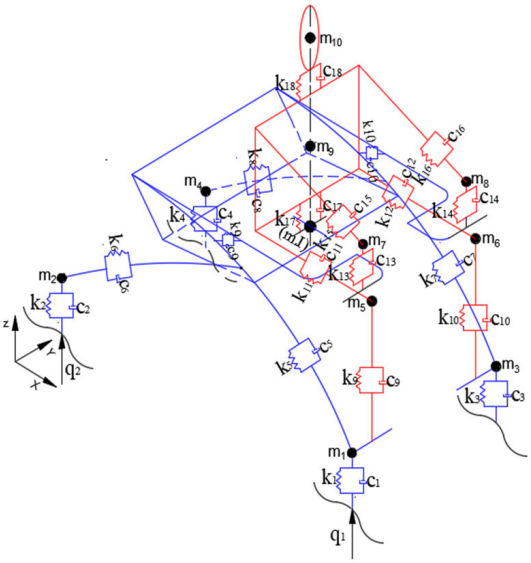

FIGURE 2. Elder-robot couple model.

The following are the generalized coordinates:

$$\{q\} = \left\{ \begin{array}{l} z_1, z_2, z_3, z_4, z_5, z_6, z_7, z_8, \\ z_9, z_{10}, z_{11}, z_{12}, z, \theta \end{array} \right\} \tag{1}$$

where z_1, z_2, z_3, and z_4 are the vertical displacements of the robot wheels. It can be assumed that the vibrations of the two front or rear wheels are identical, i.e., $(z_1 = z_3)$ and $(z_2 = z_4)$. Also, z_5 & z_6, z_7 & z_8 are the vertical displacements of the elder legs and hands, respectively. It can be assumed that the vibrations of the two legs or hands are identical, i.e., $(z_5 = z_6)$ and $(z_7 = z_8)$. In addition, z_9 and z_{10} are the vertical displacements of the elder's body and head, respectively. z is the vertical displacement of the robot's body, and θ is the rotation angle of the robot about Y-Axis.

When the external disturbances (q_1 and q_2) acted on the robot, the length d and tilt angle β of the tilt springs and dampers for the robot-elder couple system changed by Δd and $\Delta\beta$, respectively, as shown in Fig. 3. This change is caused due to the movements of point A and B by different displacements of z_i and z_{i+1}, respectively. Using trigonometry, the Δd, vertical spring force, and vertical damping force

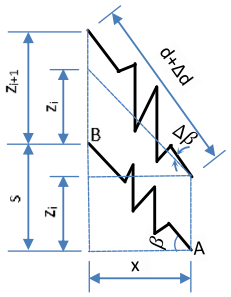

FIGURE 3. Extension displacement of tilt spring.

can be illustrated in equations 2, 3, and 4, respectively.

$$\Delta d = \frac{s}{d}(z_{i+1} - z_i) \tag{2}$$

$$F_s = k\Delta d \ \sin\beta = kl_i(z_{i+1} - z_i) \tag{3}$$

$$F_D = cl_i(\dot{z}_{i+1} - \dot{z}_i) \tag{4}$$

where $l_i = (s/d)\sin\beta$, c is the damping coefficient, and k is the spring stiffness. After preliminary measurement of the system, it's found that $l_1 = (s_1/d_1)\sin\beta_1 = 0.3$m, $l_2 = (s_2/d_2)\sin\beta_2 = 0.419$m, $l_3 = (s_3/d_3)\sin\beta_3 = 0.011$m, $l_8 = (s_8/d_8)\sin\beta_8 = 0.264$m, $l_9 = (s_9/d_9)\sin\beta_9 = 0.132$m, l_6(the length of robot arm starting at the arm-robot fixed point and ending at the arm-actuator intersection point) = 0.4m, l_7(robot arm length) = 0.81m, l_{10}(the distance between the robot center of gravity and the effectiveness point of the robot leg)=0.02m, l_{11}(the distance between the robot center of gravity and the elder sit point)=0.1m, l(the distance between the robot center of gravity and robot-arm actuator intersection point) = 0.14m.

$$\begin{aligned}
&m_1\ddot{z}_1 + (c_1 + c_5l_1 + c_9)\dot{z}_1 - c_9\dot{z}_5 - c_5l_1\dot{z} - c_5l_1l_{10}\dot{\theta} \\
&\quad + (k_1 + k_5l_1 + k_9)z_1 - k_9z_5 - k_5l_1z - k_5l_1l_{10}\theta \\
&= c_1\dot{q}_1 + k_1q_1
\end{aligned} \tag{5}$$

$$\begin{aligned}
&m_2\ddot{z}_2 + (c_2 + c_6l_2)\dot{z}_2 - c_6l_2\dot{z} + c_6l_2l_{10}\dot{\theta} \\
&\quad + (k_2 + k_6l_2)z_2 - k_6l_2z + k_6l_2l_{10}\theta = c_2\dot{q}_2 + k_2q_2
\end{aligned} \tag{6}$$

$$\begin{aligned}
&m_3\ddot{z}_3 + (c_3 + c_7l_1 + c_{10})\dot{z}_3 - c_{10}\dot{z}_6 - c_7l_1\dot{z} \\
&\quad - c_7l_1l_{10}\dot{\theta} + (k_3 + k_7l_1 + k_{10})z_3 - k_{10}z_6 \\
&\quad -k_7l_1z - k_7l_1l_{10}\theta = c_3\dot{q}_3 + k_3q_3
\end{aligned} \tag{7}$$

$$\begin{aligned}
&m_4\ddot{z}_4 + (c_4 + c_8l_2)\dot{z}_2 - c_8l_2\dot{z} + c_8l_2l_{10}\dot{\theta} \\
&\quad + (k_4 + k_8l_2)z_2 - k_8l_2z + k_8l_2l_{10}\theta = c_4\dot{q}_2 + k_4q_2
\end{aligned} \tag{8}$$

$$\begin{aligned}
&m_5\ddot{z}_5 - c_9\dot{z}_1 + (c_9 + c_{11}l_3)\dot{z}_5 - c_{11}l_3\dot{z}_9 \\
&\quad - k_9z_1 + (k_9 + k_{11}l_3)z_5 - k_{11}l_3z_9 = 0
\end{aligned} \tag{9}$$

$$\begin{aligned}
&m_6\ddot{z}_6 - c_{10}\dot{z}_3 + (c_{10} + c_{12}l_3)\dot{z}_6 - c_{12}l_3\dot{z}_9 \\
&\quad - k_{10}z_3 + (k_{10} + k_{12}l_3)z_6 - k_{12}l_3z_9 = 0
\end{aligned} \tag{10}$$

$$\begin{aligned}
&m_7\ddot{z}_7 + (c_{13} + c_{15}l_8)\dot{z}_7 - c_{15}l_8\dot{z}_9 - pc_{13}\dot{z}_{11} \\
&\quad + (k_{13} + k_{15}l_8)z_7 - k_{15}l_8z_9 - pk_{13}z_{11} = 0
\end{aligned} \tag{11}$$

$$\begin{aligned}
&m_8\ddot{z}_8 + (c_{14} + c_{16}l_8)\dot{z}_8 - c_{16}l_8\dot{z}_9 - pc_{14}\dot{z}_{12} \\
&\quad + (k_{14} + k_{16}l_8)z_8 - k_{16}l_8z_9 - pk_{14}z_{12} = 0
\end{aligned} \tag{12}$$

$$\begin{aligned}
&m_9\ddot{z}_9 - c_{11}l_3\dot{z}_5 - c_{12}l_3\dot{z}_6 - c_{15}l_8\dot{z}_7 - c_{16}l_8\dot{z}_8 + h_1\dot{z}_9 \\
&\quad -c_{18}\dot{z}_{10} - c_{17}\dot{z} - c_{17}l_{11}\dot{\theta} - k_{11}l_3z_5 - k_{12}l_3z_6 - k_{15}l_8z_7 \\
&\quad - k_{16}l_8z_8 + n_1z_9 - k_{18}z_{10} - c_{17}z - k_{17}l_{11}\theta = 0
\end{aligned} \tag{13}$$

$$m_{10}\ddot{z}_{10} - c_{18}\dot{z}_9 + c_{18}\dot{z}_{10} - k_{18}z_9 + k_{18}z_{10} = 0 \tag{14}$$

$$\begin{aligned}
&m_{11}\ddot{z}_{11} - pc_{13}\dot{z}_7 + [p^2c_{13} + c_{19}l_9]\dot{z}_{11} - l_9c_{19}\dot{z} \\
&\quad + ll_9c_{19}\dot{\theta} - pk_{13}z_7 + [p^2k_{13} + k_{19}l_9]z_{11} - l_9k_{19}\dot{z} \\
&\quad + ll_9k_{19}\theta = 0
\end{aligned} \tag{15}$$

$$\begin{aligned}
&m_{12}\ddot{z}_{12} - pc_{14}\dot{z}_8 + [p^2c_{14} + c_{20}l_9]\dot{z}_{12} - l_9c_{20}\dot{z} \\
&\quad + ll_9c_{20}\dot{\theta} - pk_{14}z_8 + [p^2k_{14} + k_{20}l_9]z_{12} - l_9k_{20}\dot{z} \\
&\quad + ll_9k_{20}\theta = 0
\end{aligned} \tag{16}$$

$$\begin{aligned}
&m\ddot{z} - c_5l_1\dot{z}_1 - c_7l_1\dot{z}_3 - c_6l_2\dot{z}_2 - c_8l_2\dot{z}_4 - c_{17}\dot{z}_9 \\
&\quad -c_{19}l_9\dot{z}_{11} - c_{20}l_9\dot{z}_{12} + h_2\dot{z} - h_3\dot{\theta} - k_5l_1z_1 - k_7l_1z_3 \\
&\quad - k_6l_2z_2 - k_8l_2z_4 - k_{17}z_9 - k_{19}l_9z_{11} - k_{20}l_9z_{12} \\
&\quad + n_2z - n_3\theta = 0
\end{aligned} \tag{17}$$

$$\begin{aligned}
&I\ddot{\theta} - c_5l_{10}l_1\dot{z}_1 - c_7l_{10}l_1\dot{z}_3 - c_6l_{10}l_2\dot{z}_2 - c_8l_{10}l_2\dot{z}_4 \\
&\quad - c_{17}l_{11}\dot{z}_9 + c_{19}ll_9\dot{z}_{11} + c_{20}ll_9\dot{z}_{12} - h_4\dot{z} + h_5\dot{\theta} \\
&\quad -k_5l_{10}l_1z_1 - k_7l_{10}l_1z_3 - k_6l_{10}l_2z_2 + k_8l_{10}l_2z_4 \\
&\quad -k_{17}l_{11}z_9 + k_{19}ll_9z_{11} + k_{20}ll_9z_{12} - n_4z + n_5\theta = 0
\end{aligned} \tag{18}$$

Thus, the final equations of motion for the elder-robot couple system can be derived using Newton's second law, as shown in Eq. (5) to Eq. (18). Where p, h_1, h_2, h_3, h_4, h_5, n_1, n_2, n_3, n_4, and n_5 are constants and presented in appendix.

Finally, the derived dynamic equations can be expressed using Eq. (19)

$$M\ddot{z} + C\dot{z} + Kz = b_1\dot{q} + b_2q \tag{19}$$

M, C, and K are the mass, damping, and stiffness matrices, respectively. However, b_1 and b_2 are the input matrices. Using data in Table 1, the numerical values of M, C, K, b_1, and b_2 will be shown in Appendix.

1) MODEL SIMULATION

To analyze the dynamic behavior of the robot-elder system, a simulation using Matlab software was conducted for different road roughness and robot speeds. To begin with, a 32-year-old, 71.8kg male subject is adopted as the case study for the experimental analysis in this study. Also, the parameters of Eq. (19) need to be calculated for the simulation analysis. Thus, the Coinv DASP V10 DAQ set-up shown in Fig. 4 was used for the experimental parameter identification of the physical prototype. After the modal analysis of each part of the system, the simulation parameters were determined and listed in Table 1. Moreover, the human-robot system will vibrate when it runs on an uneven road. Hence, the responses in the coupled part's time and frequency domains under different road surfaces can be analyzed as described below. The road roughness can be mathematically expressed as presented in [45], [46], and [47]. In this work, the road spectrum for The simulation analysis was generated by filtering white noise as expressed in Eq. (20) [48], [49].

$$\dot{q}(t) = -2\pi f_0q(t) + 2\pi\sqrt{G_dv}\omega(t) \tag{20}$$

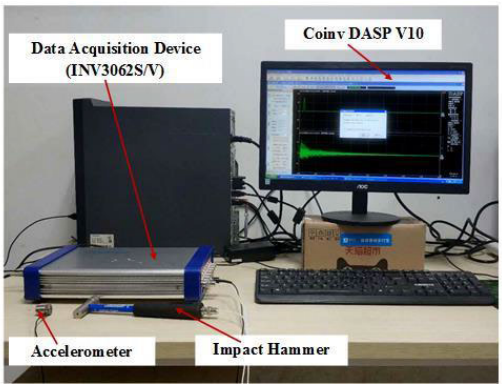

FIGURE 4. Coinv DASP V10 by china orient institute of noise & vibration.

(a) (b)

FIGURE 5. a) Block road, b) Asphalt road.

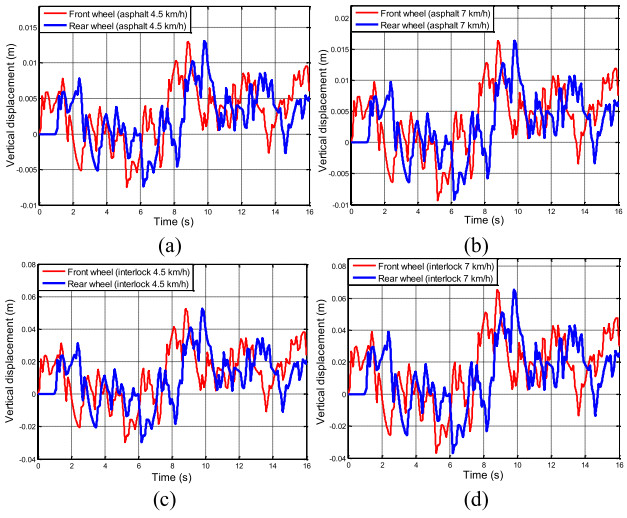

(a) (b) (c) (d)

FIGURE 6. Uneven road excitation: a) Asphalt Road (4.5 km/h), b) Asphalt Road (7 km/h), c) Interlock (4.5 km/h), d) interlock Road (7 km/h).

where $q(t)$ is a column vector with input displacements of the front and rear wheels, $\dot{q}(t)$ is a column vector comprised of zero-mean white noise, f_0 is a lower cut-off frequency ($f_0 = 0.0628$Hz), v is the robot's speed, and G_d is the road roughness coefficient. The road roughness excitation of the rear wheels lags relative to the front wheels. Thus, the road excitation signals of Fig. 5 for the robot's front and rear wheels can be generated, as shown in Fig. 6.

TABLE 1. Parameters of elder-robot couple system.

Symbol	Parameter	Value[unit]
m	robot mass	77.9 [kg]
I	robot inertia	35.3 [kg.m^2]
$m_1 = m_3$	front wheel mass	4.5 [kg]
$m_2 = m_4$	rear wheel mass	1.7 [kg]
$m_5 = m_6$	elder leg mass	4.31 [kg]
$m_7 = m_8$	elder hand mass	4.16 [kg]
m_9	elder body mass	49.8 [kg]
m_{10}	elder head mass	5.1 [kg]
$m_{11} = m_{12}$	robot arm mass	3.25 [kg]
$K_1 = K_3$	front wheel stiffness	6.69E4[N/m]
$K_2 = K_4$	rear wheel stiffness	1.47E5 [N/m]
$K_5 = K_7$	front leg of robot stiffness	1.94E5[N/m]
$K_6 = K_8$	rear leg of robot stiffness	4.13E5 [N/m]
$K_9 = K_{10}$	elder leg stiffness	2.64E3 [N/m]
$K_{11} = K_{12}$	elder thigh stiffness	2.29E3[N/m]
$K_{13} = K_{14}$	elder hand stiffness	1.36E3 [N/m]
$K_{15} = K_{16}$	elder arm stiffness	1.62E3 [N/m]
K_{17}	elder body stiffness	6.37E3 [N/m]
K_{18}	elder neck stiffness	6.23E4 [N/m]
$K_{19} = K_{20}$	robot arm adjustment actuator stiffness	7.31E5[N/m]
$C_1 = C_3$	front wheel damping coefficient	476.59[N.s/m]
$C_2 = C_4$	rear-wheel damping coefficient	572.41[N.s/m]
$C_5 = C_7$	front leg of robot damping coefficient	349.7[N.s/m]
$C_6 = C_8$	robot rear leg	449.5[N.s/m]
$C_9 = C_{10}$	elder leg damping coefficient	714[N.s/m]
$C_{11} = C_{12}$	elder thigh damping coefficient	378.5[N.s/m]
$C_{13} = C_{14}$	elder hand damping coefficient	293[N.s/m]
$C_{15} = C_{16}$	elder arm damping coefficient	399.03[N.s/m]
C_{17}	elder body damping coefficient	1800.25[N.s/m]
C_{18}	elder neck damping coefficient	613[N.s/m]
$C_{19} = C_{20}$	robot arm adjustment actuator damping coefficient	651[N.s/m]

III. VIBRATION ANALYSIS OF EAR SIMULATION

To perform the vibration model analysis, it is essential to check for resonance, which could affect the safety of elder people during the transporting process. Using Solidwork, the inherent frequencies of the first eight modes for the EAR couple system are (0.0477, 0.0853, 0.1364, 0.2324, 0.2862, 0.324, 0.403 and 0.4156) Hz. This work considered two different speeds of 7 km/h (F = 3.09Hz) and 4.5 km/h (F = 2Hz). There are two sources of vibration in the system; one is from the motor shaft rotation, and the other is from the uneven road. There would be no resonance when comparing the robot hub-motor output rotation frequencies with the inherent frequencies. Thus, the study's focus will be on the system's vibratory response under the road's uneven excitation. Figure 7 shows the first four modes of EAR vibration.

According to ISO 8608, the roads are classified into eight classes, from soft (A) to rough (H), as illustrated in Table 2. The dynamic model of the elder-robot couple system is

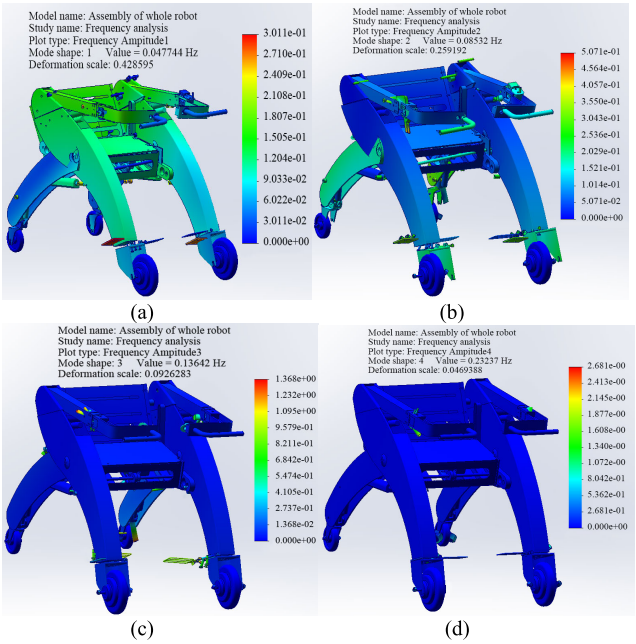

FIGURE 7. Vibration modes of EAR.

TABLE 2. ISO 8608 road classifications.

Road class	ISO 8608 Gd(Ω0)(10-6 m3/rad) $\Omega_0 = 1$ rad/m w = 2		Gd(n0)(10-6 m3/cycles) $n_0 = 0.1$ cycles /m w = 2	
	Range	Geometric mean	Range	Geometric mean
A	< 2	1	< 32	16
B	2-8	4	32-128	64
C	8-32	16	128-512	512
D	32-128	64	512-2048	1024
E	128-512	256	2048-8192	4096
F	512-2048	1024	8192-32768	16384
G	2048-8192	4096	32768-131072	65536
H	> 8192	16384	> 131072	262144

simulated and analyzed for two types of roads, namely asphalt and interlock roads, as shown in Fig. 5.

A. ASPHALT ROAD

When the EAR moves on an asphalt road, which is classified as A class road [50] ($Gd = 8 \times 10^{-6} m^3$/cycles), the robot vibrates under the excitation of the uneven road. The excitation of Eq. (20) is the input to the elder-robot couple system. Two different velocities (4.5 and 7km/h) are used to check the accuracy of the dynamic model. The excitation of the rear wheel lags from the front wheel by time t, where t is the ratio of the distance between the front and rear wheel and the robot speed (t = distance between the front and rear wheel/robot speed). The elder-robot couple system's input excitation due to the asphalt road is shown in Fig. 6(a) and Fig. 6(b).

B. INTERLOCK ROAD

The interlock road is classified as a C-class [50] ($G_d = 128 \times 10^{-6} m^3$/cycles). Due to the unevenness of the road, the elder-robot couple system will vibrate, and the dynamic model excitation for the robot for 4.5 km/h and 7 km/h are shown in Fig. 6(c) and Fig. 6(d), respectively.

C. SIMULATION RESULTS

The simulation analysis of the elder-robot system of Eq. (19) was conducted using the input excitation of Eq. (20) and Tables 1 & 2 parameters. Figures 8 and 9 show the single-sided frequency response for every part of the elder-robot system for the robot speed of 4.5 and 7km/h, respectively. According to simulation results, The dominant frequencies for the elder-robot couple system are (2.999, 3.061, 4.748, 5.061, 5.436, 16.24, 15.87, and 23.05). Comparing these frequencies with the system's inherent frequencies shown in section IV, it will be noticed that there would be no resonance during the transporting process.

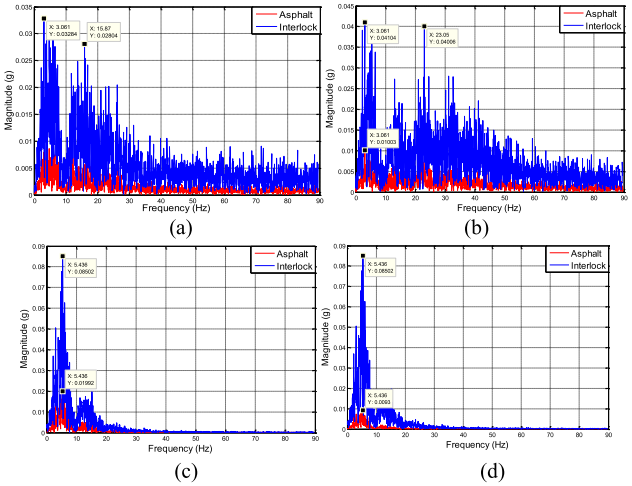

FIGURE 8. Single-sided Frequency Response with Robot speed 4.5 km/h: a) Front wheel, b) Rear wheel, c) Robot hand, d) Robot bod.

In addition, Fig. 10 shows the tilt angle of the robot during the transporting process. For all cases, the tilt angle is less than 0.167 rad (9.57 degrees), which is too little to pose any danger or trouble for the users if compared with the critical angle of robot rollover (25.3 degrees), which is calculated using Eq. (21) [47]. These simulation results show that the robot is reliable, safe, and difficult to fall during transport.

$$\theta_{cr} = \tan^{-1} \frac{B}{2h} \tag{21}$$

where B is the right and left wheel distance, h is the robot's center of gravity height.

IV. EXPERIMENTAL ANALYSIS OF EAR VIBRATION

A. EXPERIMENTAL SET-UP

The laboratory set-up used for the verification of the simulation analysis is illustrated in Fig. 11. The experimental

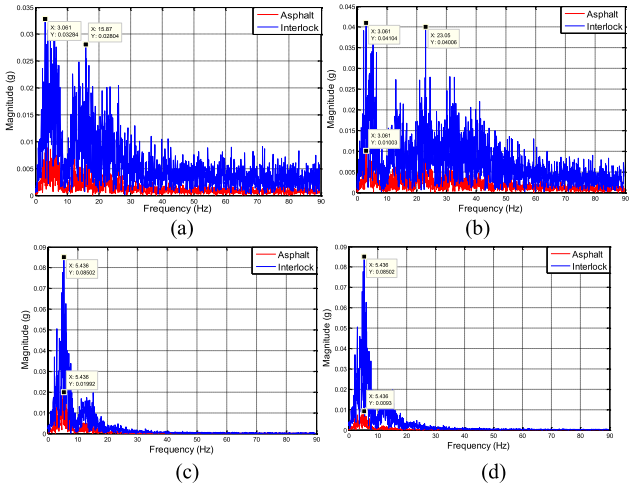

FIGURE 9. Single-sided Frequency Response with Robot speed 7 km/h: a) Front wheel, b) Rear wheel, c) Robot hand, d) Robot body.

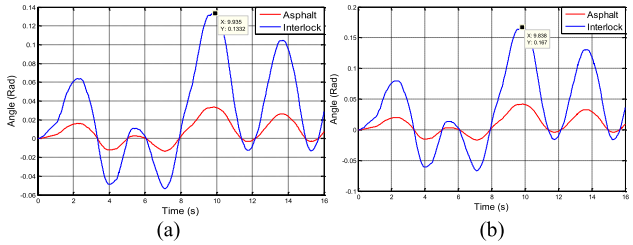

FIGURE 10. Robot Tilt Angle about Y-Axis: a) Robot Speed = 4.5km/h, b) Robot Speed = 7km/h.

study was also conducted to check the safety and discomfort of the elder assistant robot. As shown, four MPU6050 sensors (accelerometer + gyroscope) are utilized to measure 3-directional vibration as well as the tilt angle of the robot. The sensor was chosen due to its high accuracy and cost-effectiveness. The vibration sensors are placed at the following locations:

- Between the elder's hand and the robot.
- In the middle of an elder's body and the robot's seat.
- Between the elder's foot and the robot's footrest.
- In the middle of the elder's head.

According to ISO 2631-1, these points were considered to be where the vibration enters the elder's body. In addition, two speedometers were installed at the right and left front wheels to measure the robot's real-time speed. Finally, the Stm32f4 board was used as the data acquisition system to record the 3-axis vibration data of the elder-robot system at the four measurement points.

B. RESULTS AND DISCUSSION

There are numerous approaches for assessing the impact of vibration on humans. The weighted root mean square acceleration (wrms) is widely used for evaluating vibration. The crest factor, the ratio of the instantaneous maximum value to the root mean square (rms), can be utilized to check if the wrms approach is sufficient or if additional evaluation methods are needed in the evaluation process. According to ISO 2631-1, the fundamental method is suitable and adequate to evaluate the influence of vibration if the crest factor is less than or equal to nine. Figure 12 depicts the crest factor for all the measuring points for different road profiles. The crest value is always less than six, indicating that the fundamental method is adequate for evaluating the vibration of the elder-robot system.

Figures (13)–(16) show that the most considerable vibration caused by road roughness occurs in the vertical direction and is minimal in the fore and aft directions, except for the elder head, where the maximum is in the fore and aft and the least is in the vertical direction. Figure 17 shows the rms acceleration of the two roads at different robot speeds for the elderly (leg, hand, body, and head). The figure shows the transmissibility of vibration from leg to head. It is clear from Fig. 17 that the maximum vibration is at the elder's hand and leg. But the minimum is at the elder's body and head. The results demonstrated that the robot absorbed most of the induced vibration.

1) ASPHALT ROAD

Asphalt road is considered for the vibration analysis of the EAR because it is one of the most commonly used roads for transportation. The set-up of Fig. 11 was allowed to move on the asphalt road, and the responses were recorded. The vibration generated from the road roughness was transferred from the intersection point between the road and the elder robot system through the robot to the elder body.

Figure 13 (a, b) shows how the vibration entered the elder's leg for the robot speed of 4.5km/h and 7km/h, respectively. For the 4.5km/h speed, the rms vibration of the elder's leg was 0.1235g, 0.0685g, and 0.0551g for vertical, side-to-side, and fore-and-aft, respectively. When the speed increased to 7km/h, the rms acceleration increased to 0.2039g, 0.0913g, and 0.0970g, representing an increase of 65.1%, 33.28%, and 76.04%, respectively. In addition, the maximum acceleration had increased from 0.5419g to 1.0428g (+92.43%%), 0.2669g to 0.4362g (+63.43%), and 0.2395g to 0.5119g (+113.74%) for the vertical, side-to-side, and fore-and-aft, respectively.

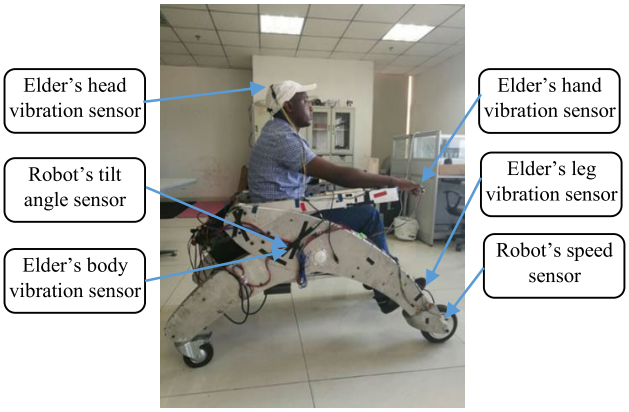

FIGURE 11. Elder-robot transporting experimental system setup.

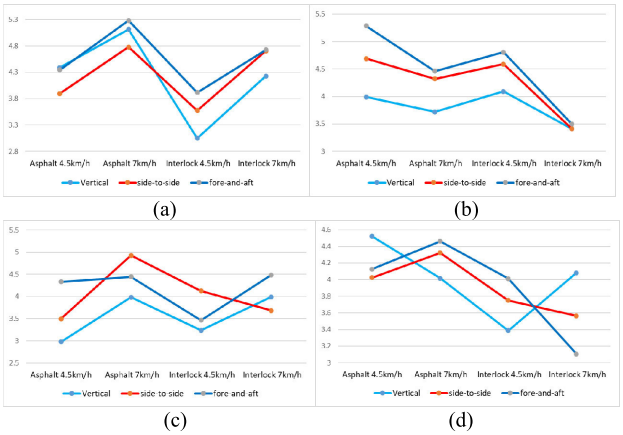

FIGURE 12. Crest factor for elder-robot system vibration: a) Elder's leg-input, b) Elder's hand-input, c) Elder's body-input, d) Elder's head.

Figure 14(a, b) shows how the vibration entered the elder's hand for the robot speed of 4.5km/h and 7km/h, respectively. The vibrations reached the elder's hand at rms accelerations of 0.2408g, 0.1774g, and 0.1311g for vertical, side-to-side, and fore-and-aft accordingly at a robot speed of 4.5km/h. The rms climbed to 0.3424g, 0.2268g, and 0.1670g when the speed was increased to 7km/h, representing an increase of 42.19%, 27.85%, and 27.38%, respectively. In addition, maximum vertical, side-to-side, and fore-and-aft accelerations had increased from 0.9608g to 1.273g (+32.49%), 0.8323g to 0.9802g (+17.77%) and 0.6927g to 0.7453g (+7.59%), respectively. Figure 15 (a, b) shows how the vibration entered the elder's body for robot speeds of 4.5km/h and 7km/h, respectively. The vibration enters the elder's body at rms accelerations of 0.0519g, 0.0277g, and 0.0327g for vertical, side-to-side, and fore-and-aft, respectively. The rms increased to 0.0737g, 0.0397g, and 0.0407g when the speed was increased to 7km/h, representing an increase of 42%, 43.32%, and 24.46%, respectively. In addition, the maximum acceleration had increased from 0.1546g to 0.2934g (+89.78%), 0.0969g to 0.1956g (+101.86%), and 0.1416g to 0.1809g (+27.75%) for the vertical, side-to-side and fore-and-aft, respectively. Figure 16 (a, b) shows the vibration of the elder's head for robot speeds of 4.5km/h and 7km/h, respectively. The rms accelerations of the elder's head vibration were 0.0270g, 0.0281g, and 0.0652g for vertical, side-to-side, and fore-and-aft, respectively. The rms increased to 0.0424g, 0.0397 g, and 0.0875g when the speed was increased to 7km/h, representing an increase of 57%, 41.28%, and 34.2%, respectively. In addition, the maximum acceleration had increased from 0.1221g to 0.1703g (+39.48%), 0.1131g to 0.1547g (+36.78%), and 0.2690g to 0.3101g (+15.79%) for the vertical, side-to-side and fore-and-aft, respectively.

2) INTERLOCK ROAD

Also, the vibratory response of the elder-robot system was analyzed using an interlock road, which is widely used in residential complexes and sidewalks. Figure 13 (c, d)

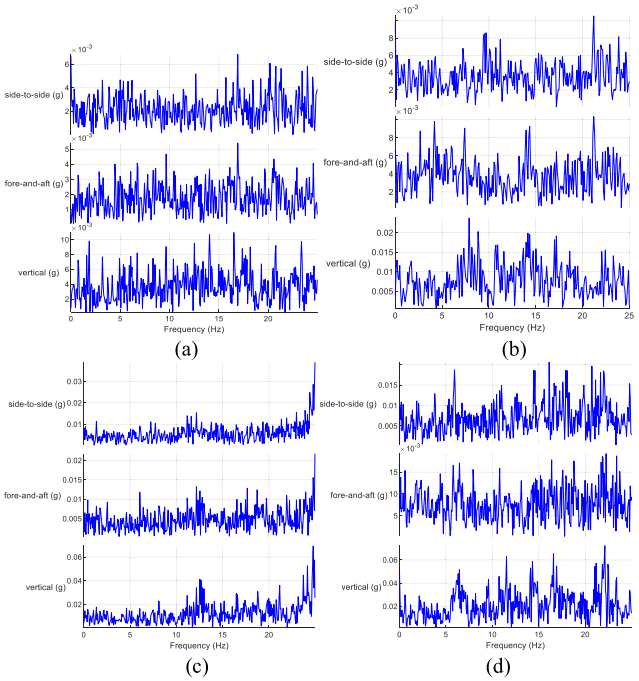

FIGURE 13. Elder's leg-input Vibration: a) Asphalt 4.5km/h, b) Asphalt 7km/h, c) Interlock 4.5km/h, d) Interlock 7km/h.

shows how the vibration entered the elder's leg for robot speeds of 4.5km/h and 7km/h, respectively. At a robot speed of 4.5km/h, the vibration enters the elder's leg at rms acceleration 0.4245g, 0.1983g, and 0.1533 for vertical, side-to-side, and fore-and-aft, respectively. The rms climbed to 0.6683g, 0.216g, and 0.2336g when the speed was increased to 7km/h, representing an increase of 57.43%, 8.93%, and 52.38%, respectively. In addition, the maximum acceleration had increased from 1.2958g to 2.8265g (+118.13%), 0.7089g to 1.0165g (+43.39%), and 0.6001g to 1.1041g (+83.99%) for the vertical, side-to-side and foreand-aft, respectively. Figure 14(c, d) shows how the vibration entered the elder's hand for robot speeds of 4.5km/h and 7km/h, respectively. Vibrations enter the elder's hand at rms accelerations of 0.5651g, 0.3648g, and 0.2569g for vertical, side-to-side, and fore-and-aft, respectively, at a robot speed of 4.5 km/h. the rms climbed to 0.8902g, 0.5535g, and 0.5793g when the speed was increased to 7km/h, representing an increase of 57.53%, 51.73%, and 125.5%, respectively.

In addition, the maximum acceleration had increased from 2.3127g to 3.0367g (+31.3%), 1.6747g to 2.0519g (+22.52%), and 1.2345g to 2.0252g (+64%) for the vertical, side-to-side and fore-and-aft, respectively.

For robot speeds of 4.5km/h and 7km/h, respectively, Fig. 15 (c, d) depicts the vibration entering the elder's body. The vibration enters the elder's body at rms accelerations of 0.2147g, 0.0647g, and 0.0849g for vertical, side-to-side, and fore-and-aft accordingly at a robot speed of 4.5 km/h. The rms increased to 0.2728g, 0.1035g, and 0.1367g when the speed was increased to 7km/h, representing an increase of

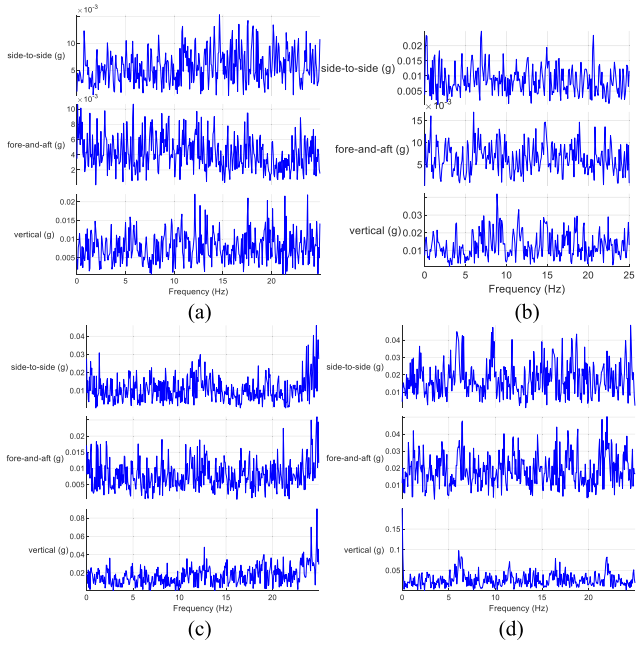

FIGURE 14. Elder's hand-input Vibration: a) Asphalt 4.5km/h, b) Asphalt 7km/h, c) Interlock 4.5km/h, d) Interlock 7km/h.

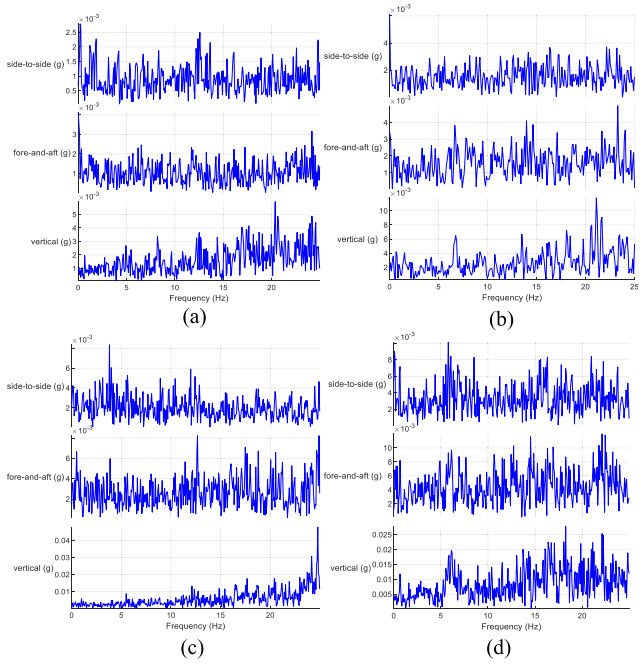

FIGURE 15. Elder's body-input Vibration: a) Asphalt 4.5km/h, b) Asphalt 7km/h, c) Interlock 4.5km/h, d) Interlock 7km/h.

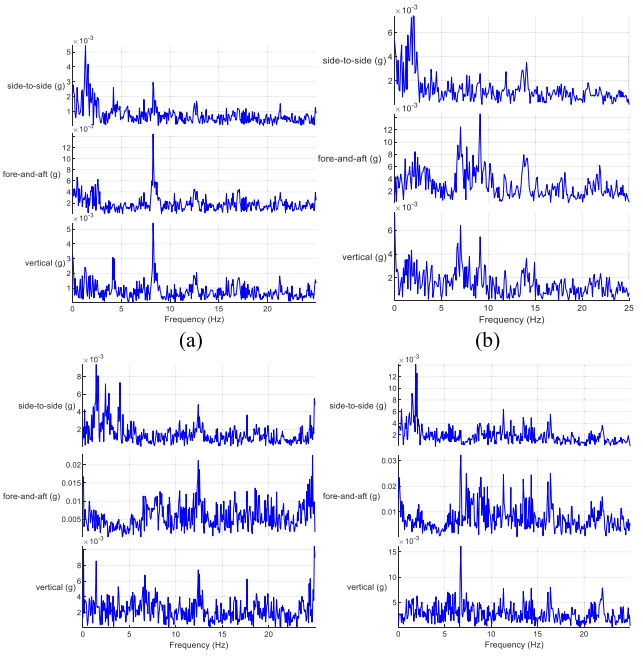

FIGURE 16. Elder's head Vibration: a) Asphalt 4.5km/h, b) Asphalt 7km/h, c) Interlock 4.5km/h, d) Interlock 7km/h.

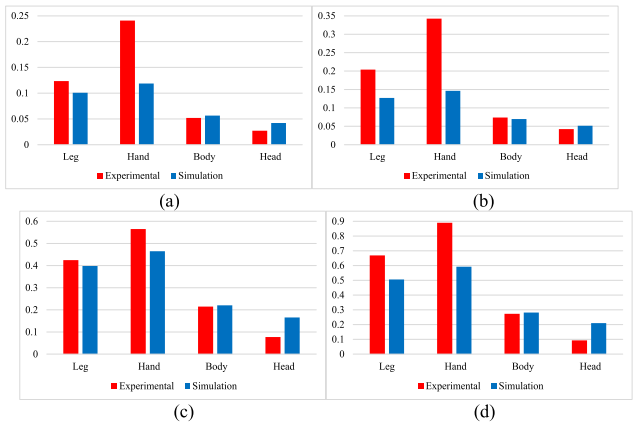

FIGURE 17. Vibration due to road roughness (rms): a) Asphalt 4.5km/h, b) Asphalt 7km/h, c) Interlock 4.5km/h, d) Interlock 7km/h.

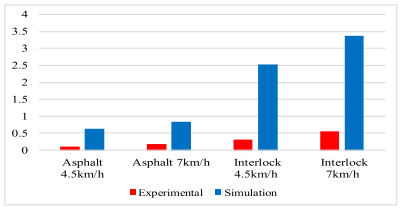

FIGURE 18. Angular speed about Y-Axis due to road roughness (rms).

27.06%, 59.97%, and 61.01%, respectively. In addition, maximum vertical, side-to-side, and fore-and-aft accelerations had increased from 0.6944g to 1.089g (+56.83%), 0.2669g to 0.3815g (+42.94%) and 0.2942g to 0.6135g (+108.53%) respectively.

The vibration of the elder's head is shown in Fig. 16 (c, d) for robot speeds of 4.5km/h and 7km/h, respectively. The rms accelerations of the elder's head vibration were 0.0772g, 0.0543g, and 0.1894g for vertical, side-to-side, and fore-and-aft, respectively, when the robot speed was 4.5km/h. The rms increased to 0.0924g, 0.0666 g, and 0.2496g when the speed was increased to 7km/h, representing an increase of 19.69%, 22.65%, and 31.78%, respectively. In addition, the maximum acceleration had increased from 0.2614g to 0.3772g (+44.3%), 0.2037g to 0.2373g (+16.49%), and 0.7598g to 0.775g (+2%) for the vertical, side-to-side and fore-and-aft, respectively.

3) MODEL VALIDATION

Figures 17 and 18 show the experimental measurement results and the Matlab simulation results in rms values. For the rms values, it's clear that the experimental results are very near to the simulation results as the vibration enters the elder's body. In addition, it's a bit far as the vibration enters the elder's hand.

The average difference between experimental and simulation results, root mean square acceleration of asphalt 4.5km/h, asphalt 7km/h, interlock 4.5km/h, and interlock 7km/h for leg-input vibration is 0.0809g, hand-input vibration is 0.15g, body-input vibration is 0.01425, and head vibration is 0.0649g. Figure 19 shows the difference between experimental and simulation results in rms acceleration for asphalt 4.5km/h, asphalt 7km/h, interlock 4.5km/h, and interlock 7km/h.

Hatano and Takahashi depicted the wheelchair user in [34] as masses joined by torsional springs and dampers; however, they represented the wheelchair as a mass with transitional springs and dampers. For a female candidate traveling at a speed of 20 km/h, a disparity between simulation and experiment is greater than 70%. The average difference between the simulation and experimental data as rms for the vibration that entered the elderly body is approximately 2.48% in this work, which is better than the difference that Yasuyoshi reported, indicating that the suggested model is more accurate.

In addition, the experimental angular speed about the Y-axis deviates from the simulation by 1.5544 degree/s as the rms average. The dynamic model effectively represents the dynamic behavior of the elder-robot system, especially for the vibration entering the elder body and elder head due to the slight difference between simulation and experimental results.

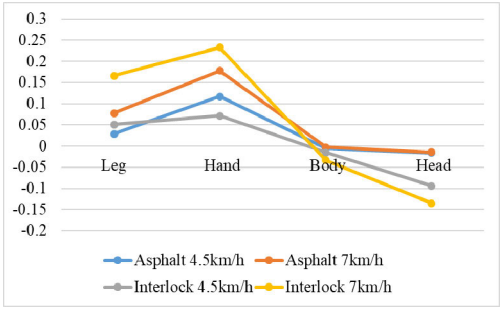

FIGURE 19. Difference between experimental and simulation results (rms).

4) COMFORTABILITY ANALYSIS

Comfortability is a significant factor for the machines used by elderly people, especially elder-assistant robots. That's due to using the robot for an extended period and the muscles decreasing, which happens with aging. According to ISO-2631-1, comfortability can be checked by calculating the weighted acceleration using Eq. (22).

$$a_w = \sqrt{a_x^2 + 1.4a_y^2 + 1.4a_z^2} \tag{22}$$

The vibration is measured on the elder-robot system without installing a suspension system, cushion, or backrest. The overall weighted root mean square accelerations based on one-third octave for asphalt road (4km/h, 7km/h) and interlock road (4km/h, 7km/h) are 0.021183m/s2, 0.034411m/s2, 0.054153m/s2, 0.240636m/s2 respectively as shown in Fig. 20. Comparing these results with the ISO 2631-1 approximate values of table 3 results all the values are less than 0.315m/s2 which mean the elder will feel comfortable on the asphalt road and interlock road at the speed of 4km/h and 7km/h without any need for suspension system or cushion.

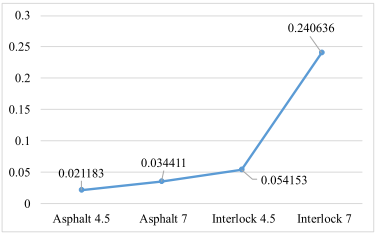

FIGURE 20. Comfortability analysis for the elder-body input vibration.

TABLE 3. ISO 2631-1 comfort approximate indications of passenger reactions to various magnitudes of overall vibration total values.

a_w (m/s²)	Human being comfortability
<0.315	comfortable
0.315 to 0.63	A little uncomfortable
0.5 to 1	Fairly uncomfortable
0.8 to 1.6	uncomfortable
1.25 to 2.5	Very uncomfortable
> 2	Extremely uncomfortable

5) VIBRATION TRANSMISSIBILITY

The vibration transmissibility of the robot is the ratio of vibration output from the robot to what input to the robot. The vibration is measured after the robot wheel, which considers the vibration entering the robot body, and then measured at the robot output, which considers the vibration entering the elder body. Transmissibility is calculated based on the root mean square acceleration. As shown in Fig. 21, the robot's vertical vibration transmissibility for asphalt 4.5 km/h, asphalt 7 km/h, interlock 4.5 km/h, and interlock 7 km/h, respectively, is 0.42, 0.361, 0.506, and 0.408. For side-to-side, the values are 0.404, 0.435, 0.326, and 0.479. For fore-and-aft, the values are 0.593, 0.42, 0.554, and 0.236.

6) SENSITIVITY ANALYSIS

To create the best possible design for the robot, sensitivity analysis examines how altering system parameters impacts the vibration of the elder-robot couple system. Matlab Simulink was used to analyze the dynamic model.

Figure 22 displays the impact of front wheel damping (C_1) and rear wheel damping (C_2) on the vertical vibration of the leg, hand, body, and head as rms.

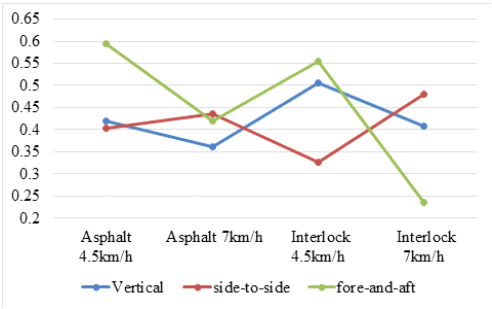

FIGURE 21. Vibration transmissibility of elder-assistant robot.

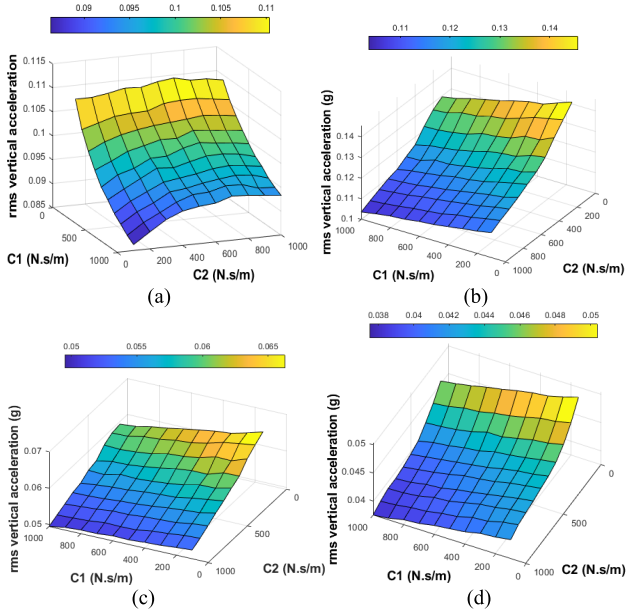

FIGURE 22. Effect of C_1 and C_2 on vertical vibration (rms): a) Leg, b) Hand, c) Body, d) Head.

A higher value for C_1 will result in less leg, hand, body, and head vibration. Additionally, increasing the value of C_2 will result in a slight increase in leg vibration while decreasing the hand, body, and head vibration. Figure 22 shows that C_2 has a more significant impact on reducing vibration for the hand, body, and head than C_1.

The effect of front and rear wheel stiffness (K1 and K2) on the vertical vibration of the leg, hand, body, and head is shown in Fig. 23 as rms.

Increasing K1 will cause Less vibration in the leg, but the effect on vibration in the hand, body, and head will be minimal. Additionally, increasing the value of K2 will significantly impact the vibration of the head, body, hand, and leg. It is clear from Fig. 23 that K2 is more effective than K1 at reducing vibration in the leg, hand, body, and head.

The effect of the front leg damping (C5) and the robot's rear leg damping (C6) on the leg, hand, body, and head's vertical vibration is shown in Fig. 24 as rms.

Less leg, hand, body, and head vibration will occur from a greater value for C5. Additionally, increasing the value of C6 will cause a tiny decrease in the vibration of the hand, body, and head while slightly increasing the vibration of the leg.

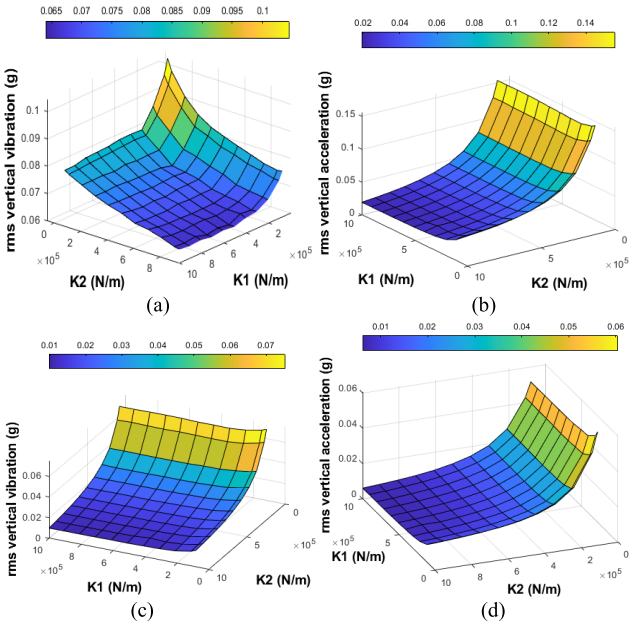

FIGURE 23. Effect of K_1 and K_2 on vertical vibration (rms): a)Leg, b) Hand, c) Body, d) Head.

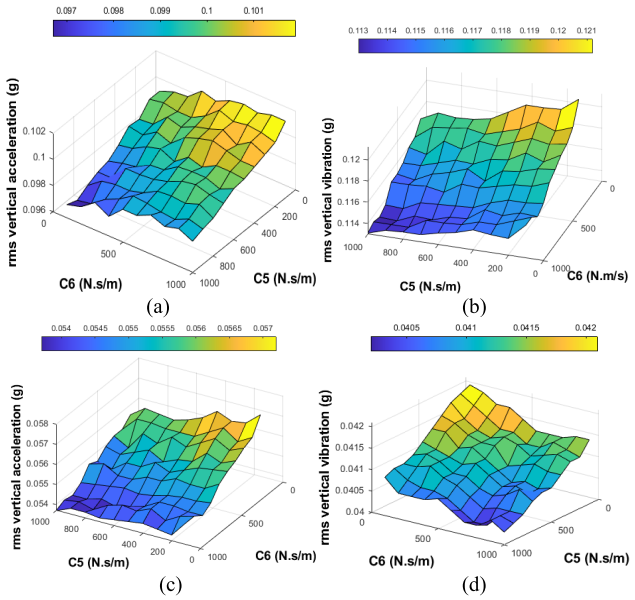

FIGURE 24. Effect of C_5 and C_6 on vertical vibration (rms): a) Leg, b) Hand, c) Body, d) Head.

It is clear from Fig. 24 that C5 affects vibration reduction for the hand, body, and head that is stronger than C6.

In Fig. 25, the rms value represents the influence of the robot's legs' stiffness (K_5 and K_6) on the vertical vibration of the leg, hand, body, and head.

Although the leg vibrates less due to increased K5 and K6, the hand, body, and head will vibrate more. K6 has less of an influence than K5, which has more.

Figure 26 displays the influence of the elder's mass and the robot's mass on the vertical vibration of the leg, hand, body, and head as rms. Less vibration will be created at all sites

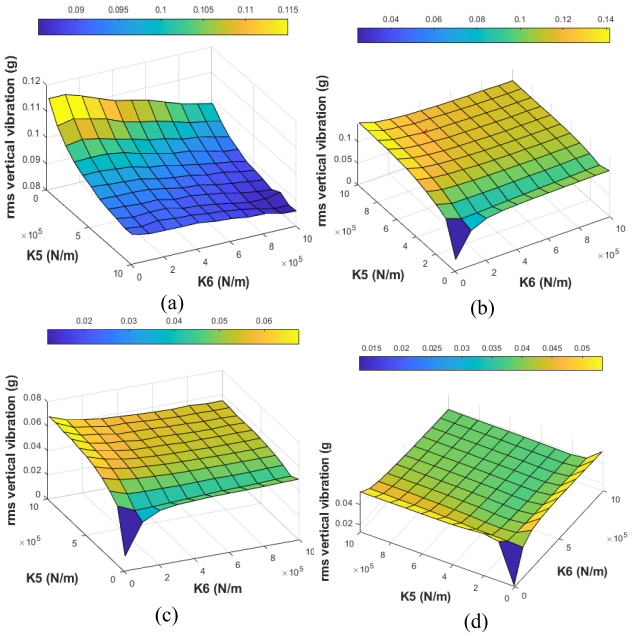

FIGURE 25. Effect of K_5 and K_6 on vertical vibration (rms): a) Leg, b) Hand, c) Body, d) Head.

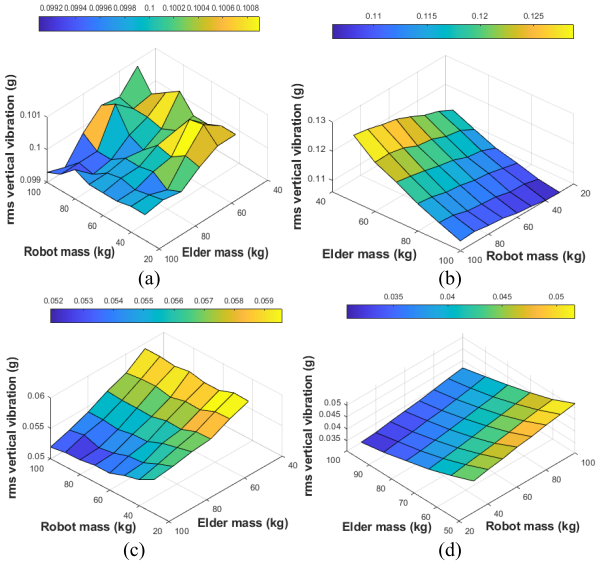

FIGURE 26. Effect of robot's mass elder's mass on vertical vibration (rms): a) Leg, b) Hand, c) Body, d) Head.

when the elder's mass increases. Additionally, all places on the robot will experience less vibration as its mass increases, except the hand, where vibration will increase. It is evident from Fig. 26 that the elder's mass is more effective in damping vibration than the robot's mass. Less than 60 kg of elder mass will result in high leg vibration in the existing design.

V. CONCLUSION

The main objective of this paper is to assess the design of an elder-assistant robot for safe application on vibration-prone roads of different roughness. The EAR structure presented in this work is a double herringbone, which acts as springs and dampers and, thus, minimizes the vibration transmission from the robot wheels to the elder's body.

The summary of the whole paper can be presented as follows:

1) A new dynamic model for the elder-EAR coupled system was derived using mass-spring-damper combinations. The model parameters, namely, damping coefficients and the spring stiffness, were experimentally determined using Coinv DASP V10.
2) The Matlab simulation analysis was conducted for different road roughness and the robot's speed. The results show that the tilt angle of the robot is less than 6 degrees for all cases. Thus, this demonstrates that the robot is safe, stable, and can prevent the elderly from falling.
3) The model was validated experimentally with two different roads, asphalt and interlock, for the robot speed of 4.5km/h and 7km/h. The results for the rms acceleration of the experimental analysis confirmed the simulation analysis, especially at the vibration entering the elder's body.
4) The ISO 2631-1 based comfortability analysis shows that the wrms acceleration for all cases is less than $0.315 m/s^2$. This demonstrated a guaranteed EAR's stability and ride comfort of the elders on both asphalt and interlock roads.
5) The transmissibility analysis shows that the robot absorbed at least 49%, 52%, and 40% of vertical, side-to-side, and fore-and-aft vibrations, respectively. This means that the robot can absorb most of the vibrations generated from the road excitation.

Finally, it can be concluded that the robot's double herringbone design has effectively decreased the vibration transmitted to the elderly and, thus, improved safety and ride comfortability. The dynamic model used in this study's simulations is very close to the experiment at the elder's body input but a little distant at the elder's leg input. Future development will, therefore, concentrate on refining the model to get more accurate results and equipping the robot with cushion and suspension systems to lessen vibration and enhance the comfort of the elderly, utilizing an active suspension system with intelligent control to improve EAR's comfort level.

APPENDIX

$$
\begin{aligned}
p &= l_7/l_6 \\
h_1 &= c_{18} + 2c_{11}l_3 + c_{17} + 2c_{15}l_8 \\
n_1 &= k_{18} + 2k_{11}l_3 + k_{17} + 2k_{15}l_8 \\
h_2 &= c_{17} + 2c_{19}l_9 + 2c_5l_1 + 2c_6l_2 \\
h_3 &= 2c_{19}ll_9 - c_{17}l_{11} - 2c_5l_{10}l_1 - 2c_6l_{10}l_2 \\
n_2 &= k_{17} + 2k_{19}l_9 + 2k_5l_1 + 2k_6l_2 \\
n_3 &= 2k_{19}ll_9 - k_{17}l_{11} - 2k_5l_{10}l_1 - 2k_6l_{10}l_2 \\
h_4 &= 2c_{19}ll_9 - c_{17}l_{11} - 2c_5l_{10}l_1 - 2c_6l_{10}l_2 \\
h_5 &= 2c_{19}l^2l_9 + c_{17}l_{11}^2 + 2c_5l_{10}^2l_1 + 2c_6l_{10}^2l_2 \\
n_4 &= 2k_{19}ll_9 - k_{17}l_{11} - 2k_5l_{10}l_1 - 2k_6l_{10}l_2 \\
n_5 &= 2k_{19}l^2l_9 + k_{17}l_{11}^2 + 2k_5l_{10}^2l_1 + 2k_6l_{10}^2l_2
\end{aligned}
$$

$$M = \begin{bmatrix}
4.5 & 0 & 0 & 0 & 0 & 0 & 0 & 0 & 0 & 0 & 0 & 0 & 0 & 0 \\
0 & 1.7 & 0 & 0 & 0 & 0 & 0 & 0 & 0 & 0 & 0 & 0 & 0 & 0 \\
0 & 0 & 4.5 & 0 & 0 & 0 & 0 & 0 & 0 & 0 & 0 & 0 & 0 & 0 \\
0 & 0 & 0 & 1.7 & 0 & 0 & 0 & 0 & 0 & 0 & 0 & 0 & 0 & 0 \\
0 & 0 & 0 & 0 & 4.31 & 0 & 0 & 0 & 0 & 0 & 0 & 0 & 0 & 0 \\
0 & 0 & 0 & 0 & 0 & 4.31 & 0 & 0 & 0 & 0 & 0 & 0 & 0 & 0 \\
0 & 0 & 0 & 0 & 0 & 0 & 4.16 & 0 & 0 & 0 & 0 & 0 & 0 & 0 \\
0 & 0 & 0 & 0 & 0 & 0 & 0 & 4.16 & 0 & 0 & 0 & 0 & 0 & 0 \\
0 & 0 & 0 & 0 & 0 & 0 & 0 & 0 & 49.8 & 0 & 0 & 0 & 0 & 0 \\
0 & 0 & 0 & 0 & 0 & 0 & 0 & 0 & 0 & 5.1 & 0 & 0 & 0 & 0 \\
0 & 0 & 0 & 0 & 0 & 0 & 0 & 0 & 0 & 0 & 3.25 & 0 & 0 & 0 \\
0 & 0 & 0 & 0 & 0 & 0 & 0 & 0 & 0 & 0 & 0 & 3.25 & 0 & 0 \\
0 & 0 & 0 & 0 & 0 & 0 & 0 & 0 & 0 & 0 & 0 & 0 & 77.9 & 0 \\
0 & 0 & 0 & 0 & 0 & 0 & 0 & 0 & 0 & 0 & 0 & 0 & 0 & 35.3
\end{bmatrix}$$

$$b_1 = \begin{bmatrix}
476.6 & 0 & 0 & 0 \\
0 & 572.4 & 0 & 0 \\
0 & 0 & 476.6 & 0 \\
0 & 0 & 0 & 572.4 \\
0 & 0 & 0 & 0 \\
0 & 0 & 0 & 0 \\
0 & 0 & 0 & 0 \\
0 & 0 & 0 & 0 \\
0 & 0 & 0 & 0 \\
0 & 0 & 0 & 0 \\
0 & 0 & 0 & 0 \\
0 & 0 & 0 & 0 \\
0 & 0 & 0 & 0 \\
0 & 0 & 0 & 0
\end{bmatrix}, \quad b_2 = 10^5 \times \begin{bmatrix}
0.669 & 0 & 0 & 0 \\
0 & 1.47 & 0 & 0 \\
0 & 0 & 0.669 & 0 \\
0 & 0 & 0 & 1.47 \\
0 & 0 & 0 & 0 \\
0 & 0 & 0 & 0 \\
0 & 0 & 0 & 0 \\
0 & 0 & 0 & 0 \\
0 & 0 & 0 & 0 \\
0 & 0 & 0 & 0 \\
0 & 0 & 0 & 0 \\
0 & 0 & 0 & 0 \\
0 & 0 & 0 & 0 \\
0 & 0 & 0 & 0
\end{bmatrix}$$

$$C = \begin{bmatrix}
1295.5 & 0 & 0 & 0 & -714 & 0 & 0 & 0 & 0 & 0 & 0 & 0 & -105 & -2.1 \\
0 & 760.8 & 0 & 0 & 0 & 0 & 0 & 0 & 0 & 0 & 0 & 0 & -188.3 & -3.8 \\
0 & 0 & 1295.5 & 0 & 0 & -714 & 0 & 0 & 0 & 0 & 0 & 0 & -105 & -2.1 \\
0 & 0 & 0 & 760.8 & 0 & 0 & 0 & 0 & 0 & 0 & 0 & 0 & -188.3 & -3.8 \\
-714 & 0 & 0 & 0 & 718.2 & 0 & 0 & 0 & -4.2 & 0 & 0 & 0 & 0 & 0 \\
0 & 0 & -714 & 0 & 0 & 718.2 & 0 & 0 & -4.2 & 0 & 0 & 0 & 0 & 0 \\
0 & 0 & 0 & 0 & 0 & 0 & 398.3 & 0 & -105.3 & 0 & -593.3 & 0 & 0 & 0 \\
0 & 0 & 0 & 0 & 0 & 0 & 0 & 398.3 & -105.3 & 0 & 0 & -593.3 & 0 & 0 \\
0 & 0 & 0 & 0 & -4.2 & -4.2 & -105.3 & -105.3 & 2632.3 & -613 & 0 & 0 & -1800.3 & -180 \\
0 & 0 & 0 & 0 & 0 & 0 & 0 & 0 & -613 & 613 & 0 & 0 & 0 & 0 \\
0 & 0 & 0 & 0 & 0 & 0 & -593.3 & 0 & 0 & 0 & 1287.4 & 0 & -85.9 & 12 \\
0 & 0 & 0 & 0 & 0 & 0 & 0 & -593.3 & 0 & 0 & 0 & 1287.4 & -85.9 & 12 \\
-105 & -188.3 & -105 & -188.3 & 0 & 0 & 0 & 0 & -1800.3 & 0 & -85.9 & -85.9 & 2558.6 & 167.7 \\
-2.1 & -3.8 & -2.1 & -3.8 & 0 & 0 & 0 & 0 & -180 & 0 & 12 & 12 & 167.7 & 21.6
\end{bmatrix}$$

$$K = 10^5 * \begin{bmatrix}
1.2774 & 0 & 0 & 0 & -0.0264 & 0 & 0 & 0 & 0 & 0 & 0 & 0 & -0.5820 & -0.0116 \\
0 & 3.2004 & 0 & 0 & 0 & 0 & 0 & 0 & 0 & 0 & 0 & 0 & -1.7304 & -0.0346 \\
0 & 0 & 1.2774 & 0 & 0 & -0.0264 & 0 & 0 & 0 & 0 & 0 & 0 & -0.5820 & -0.0116 \\
0 & 0 & 0 & 3.2004 & 0 & 0 & 0 & 0 & 0 & 0 & 0 & 0 & -1.7304 & -0.0346 \\
-0.0264 & 0 & 0 & 0 & 0.0267 & 0 & 0 & 0 & -0.0003 & 0 & 0 & 0 & 0 & 0 \\
0 & 0 & -0.0264 & 0 & 0 & 0.0267 & 0 & 0 & -0.0003 & 0 & 0 & 0 & 0 & 0 \\
0 & 0 & 0 & 0 & 0 & 0 & 0.0179 & 0 & -0.0043 & 0 & -0.0275 & 0 & 0 & 0 \\
0 & 0 & 0 & 0 & 0 & 0 & 0 & 0.0179 & -0.0043 & 0 & 0 & -0.0275 & 0 & 0 \\
0 & 0 & 0 & 0 & -0.0003 & -0.0003 & -0.0043 & -0.0043 & 0.6957 & -0.6230 & 0 & 0 & -0.0637 & -0.0064 \\
0 & 0 & 0 & 0 & 0 & 0 & 0 & 0 & -0.6230 & 0.6230 & 0 & 0 & 0 & 0 \\
0 & 0 & 0 & 0 & 0 & 0 & -0.0275 & 0 & 0 & 0 & 1.0259 & 0 & -0.9649 & 0.1351 \\
0 & 0 & 0 & 0 & 0 & 0 & 0 & -0.0275 & 0 & 0 & 0 & 1.0207 & -0.9649 & 0.1351 \\
-0.5820 & -1.7305 & -0.5820 & -1.7305 & 0 & 0 & 0 & 0 & -0.0637 & 0 & -0.9649 & -0.9649 & 6.6150 & -0.1713 \\
-0.0116 & -0.0346 & -0.0116 & -0.0346 & 0 & 0 & 0 & 0 & -0.0064 & 0 & 0.1351 & 0.1351 & -0.1713 & 0.0403
\end{bmatrix}$$

REFERENCES

[1] S. Amarya, K. Singh, and M. Sabharwal, "Ageing process and physiological changes," in *Gerontology*. London, U.K.: InTech, 2018, doi: 10.5772/intechopen.76249.

[2] G. Valdez, "Effects of disease-afflicted and aging neurons on the musculoskeletal system," *Bone*, vol. 122, pp. 31–37, May 2019, doi: 10.1016/j.bone.2019.01.023.

[3] *United Nations, Department of Economic and Social Affairs, Population Division*, World Population Ageing 2019 (ST/ESA/SER.A/444), New York, NY, USA, 2020.

[4] *World Report on Disability*, World Health Org. & World Bank, Geneva, Switzerland, 2011.

[5] A. L. Ward, S. Hammond, S. Holsten, E. Bravver, and B. R. Brooks, "Power wheelchair use in persons with amyotrophic lateral sclerosis: Changes over time," *Assistive Technol.*, vol. 27, no. 4, pp. 238–245, Oct. 2015, doi: 10.1080/10400435.2015.1040896.

[6] A. Vitanza, G. D'Onofrio, F. Ricciardi, D. Sancarlo, A. Greco, and F. Giuliani, "Assistive robots for the elderly: Innovative tools to gather health relevant data," in *Data Science for Healthcare*. Cham, Switzerland: Springer, 2019, pp. 195–215, doi: 10.1007/978-3-030-05249-2_7.

[7] Q. Yan, J. Huang, C. Tao, X. Chen, and W. Xu, "Intelligent mobile walking-aids: Perception, control and safety," *Adv. Robot.*, vol. 34, no. 1, pp. 2–18, Jan. 2020, doi: 10.1080/01691864.2019.1653225.

[8] N. Chen, J. Song, and B. Li, "Providing aging adults social robots' companionship in home-based elder care," *J. Healthcare Eng.*, vol. 2019, pp. 1–7, Jun. 2019, doi: 10.1155/2019/2726837.

[9] G. Yang, H. Lv, F. Chen, Z. Pang, J. Wang, H. Yang, and J. Zhang, "A novel gesture recognition system for intelligent interaction with a nursing-care assistant robot," *Appl. Sci.*, vol. 8, no. 12, p. 2349, Nov. 2018, doi: 10.3390/app8122349.

[10] S. Park, J. Kim, and Y. Won, "An efficient electronic wheelchair seat balancing maintain methodology applying smart sensors," *Int. J. Smart Home*, vol. 9, no. 1, pp. 81–92, Jan. 2015, doi: 10.14257/ijsh.2015.9.1.09.

[11] A. S. Kundu, O. Mazumder, P. K. Lenka, and S. Bhaumik, "Design and performance evaluation of 4 wheeled omni wheelchair with reduced slip and vibration," *Proc. Comput. Sci.*, vol. 105, pp. 289–295, Jan. 2017, doi: 10.1016/j.procs.2017.01.224.

[12] S. Lefèvre, A. Carvalho, and F. Borrelli, "A learning-based framework for velocity control in autonomous driving," *IEEE Trans. Autom. Sci. Eng.*, vol. 13, no. 1, pp. 32–42, Jan. 2016, doi: 10.1109/TASE.2015.2498192.

[13] E. Ceravolo, M. Gabellone, M. Farina, L. Bascetta, and M. Matteucci, "Model predictive control of an autonomous wheelchair," *IFAC-PapersOnLine*, vol. 50, no. 1, pp. 9821–9826, Jul. 2017, doi: 10.1016/j.ifacol.2017.08.894.

[14] Y. Morales, N. Kallakuri, K. Shinozawa, T. Miyashita, and N. Hagita, "Human-comfortable navigation for an autonomous robotic wheelchair," in *Proc. IEEE/RSJ Int. Conf. Intell. Robots Syst.*, Nov. 2013, pp. 2737–2743, doi: 10.1109/IROS.2013.6696743.

[15] Y. Morales, T. Miyashita, and N. Hagita, "Social robotic wheelchair centered on passenger and pedestrian comfort," *Robot. Auto. Syst.*, vol. 87, pp. 355–362, Jan. 2017, doi: 10.1016/j.robot.2016.09.010.

[16] V. T. Nguyen, C. Jayawardena, and I. Ardekani, "A navigation model for side-by-side robotic wheelchairs for optimizing social comfort in crossing situations," *Robot. Auto. Syst.*, vol. 100, pp. 27–40, Feb. 2018, doi: 10.1016/j.robot.2017.10.008.

[17] G. B. Kamalakar and A. C. Mitra, "Development and analysis of human hand-arm system model for anti-vibration isolators," *Mater. Today, Proc.*, vol. 5, no. 2, pp. 3943–3952, 2018, doi: 10.1016/j.matpr.2017.11.651.

[18] S. Wang, L. Zhao, Y. Hu, and F. Yang, "Vibration characteristics analysis of convalescent-wheelchair robots equipped with dynamic absorbers," *Shock Vibrat.*, vol. 2018, no. 1, Jan. 2018, Art. no. 5393051, doi: 10.1155/2018/5393051.

[19] S. Wang, L. Zhao, Y. Hu, and F. Yang, "Impact responses and parameters sensitivity analysis of electric wheelchairs," *Electronics*, vol. 7, no. 6, p. 87, Jun. 2018, doi: 10.3390/electronics7060087.

[20] M. Hischke and R. F. Reiser, "Effect of rear wheel suspension on tilt-in-space wheelchair shock and vibration attenuation," *PM R*, vol. 10, no. 10, pp. 1040–1050, Oct. 2018, doi: 10.1016/j.pmrj.2018.02.009.

[21] K.-H. Su, T.-H. Chang, and S.-F. Su, "Design of fuzzy-based magnetic suspension vibrator for electric wheelchair," in *Proc. IEEE 12th Int. Conf. Netw., Sens. Control*, Apr. 2015, pp. 586–591, doi: 10.1109/ICNSC.2015.7116103.

[22] S. J. Hillman, J. Hollington, N. Crossan, and C. Torres-Sánchez, "Correlation of ISO 16840–2:2007 impact damping and hysteresis measures for a sample of wheelchair seating cushions," *Assistive Technol.*, vol. 30, no. 2, pp. 77–83, Mar. 2018, doi: 10.1080/10400435.2016.1261963.

[23] D. Brienza, J. Vallely, P. Karg, J. Akins, and A. Gefen, "An MRI investigation of the effects of user anatomy and wheelchair cushion type on tissue deformation," *J. Tissue Viability*, vol. 27, no. 1, pp. 42–53, Feb. 2018, doi: 10.1016/j.jtv.2017.04.001.

[24] X. Zhang, Y. Qiu, and M. J. Griffin, "Transmission of vertical vibration through a seat: Effect of thickness of foam cushions at the seat pan and the backrest," *Int. J. Ind. Ergonom.*, vol. 48, pp. 36–45, Jul. 2015, doi: 10.1016/j.ergon.2015.03.006.

[25] C.-C. Liang and C.-F. Chiang, "Modeling of a seated human body exposed to vertical vibrations in various automotive postures," *Ind. Health*, vol. 46, no. 2, pp. 125–137, 2008, doi: 10.2486/indhealth.46.125.

[26] C. Zhang, X. Meng, D. E. Anderson, W. Wang, X. Tao, and B. Cheng, "Effects of stretch reflex on back muscle response during sinusoidal whole body vibration in sitting posture: A model study," *Int. J. Ind. Ergonom.*, vol. 71, pp. 103–110, May 2019, doi: 10.1016/j.ergon.2019.02.005.

[27] J. Wu and Y. Qiu, "Modelling of seated human body exposed to combined vertical, lateral and roll vibrations," *J. Sound Vibrat.*, vol. 485, Oct. 2020, Art. no. 115509, doi: 10.1016/j.jsv.2020.115509.

[28] Y. Matsuoka, "Vibration analysis and design problems of the vehicles modified with the wheelchair transporting apparatus," *KANSEI Eng. Int.*, vol. 1, no. 3, pp. 39–46, 2000, doi: 10.5057/kei.1.3_39.

[29] Y. Matsuoka, "Vibration simulation model for the transportation of wheelchair-bound passengers," *KANSEI Eng. Int.*, vol. 1, no. 3, pp. 47–52, 2000, doi: 10.5057/kei.1.3_47.

[30] Y. Matsuoka, "Vibration evaluation model on the wheelchair transporting apparatus," *KANSEI Eng. Int.*, vol. 1, no. 3, pp. 53–60, 2000, doi: 10.5057/kei.1.3_53.

[31] D. Yamagami, Y. Sato, Y. Noda, T. Miyoshi, and K. Terashima, "Wheelchair driving control with passenger's posture behavior suppression and evaluation of comfort of ride by emotional sweating," in *Proc. Int. Conf. Adv. Comput. Control*, 2009, pp. 30–35, doi: 10.1109/icacc.2009.74.

[32] A. Kawaguchi, J. Wei, Y. Noda, T. Miyoshi, and K. Terashima, "A study on the safety and drivability enhancement of mobile wheelchairs," in *Proc. Int. Conf. Comput., Eng. Inf.*, Apr. 2009, pp. 384–387, doi: 10.1109/ICC.2009.68.

[33] J.-J. Huang, H.-H. Chiang, T.-T. Lee, and K.-Y. Kou, "Riding comfort improvement by considering passenger's behavior suppression on powered wheelchairs," in *Proc. Int. Conf. Syst. Sci. Eng. (ICSSE)*, Jun. 2012, pp. 131–136, doi: 10.1109/ICSSE.2012.6257163.

[34] Y. Hatano and M. Takahashi, "Design and experimental verification of vibration suppression device on the lift of wheelchair-accessible vehicles," *J. Phys., Conf.*, vol. 744, Sep. 2016, Art. no. 012221, doi: 10.1088/1742-6596/744/1/012221.

[35] Y. Matsuoka, K. Kawai, and R. Sato, "Vibration simulation model of passenger-wheelchair system in wheelchair-accessible vehicle," *J. Mech. Des.*, vol. 125, no. 4, pp. 779–785, Dec. 2003, doi: 10.1115/1.1631442.

[36] K. K. Hamza, X. Zhang, X. Mu, and O. R. Osivue, "Vibration analysis of transporting elderly posture behavior of elderly-assistant and walking-assistant robot considering elderly falling angle," in *Proc. IEEE Int. Conf. Power, Intell. Comput. Syst. (ICPICS)*, Jul. 2020, pp. 730–734, doi: 10.1109/ICPICS50287.2020.9201973.

[37] K. Brown, H. Flashner, J. McNitt-Gray, and P. Requejo, "Modeling wheelchair-users undergoing vibrations," *J. Biomechanical Eng.*, vol. 139, no. 9, Sep. 2017, Art. no. 094501, doi: 10.1115/1.4037220.

[38] M. F. Hikmawan and A. S. Nugraha, "Analysis of electric wheelchair passanger comfort with a half car model approach," in *Proc. Int. Conf. Sustain. Energy Eng. Appl. (ICSEEA)*, Oct. 2016, pp. 76–80, doi: 10.1109/ICSEEA.2016.7873571.

[39] K. Kadry Hamza, X. Zhang, X. Mu, R. Odekhe, and A. B. Alhassan, "Modeling and simulation of transporting elderly posture of multifunctional elderly-assistant and walking-assistant robot," in *Proc. IEEE 8th Annu. Int. Conf. CYBER Technol. Autom., Control, Intell. Syst. (CYBER)*, Jul. 2018, pp. 822–826, doi: 10.1109/CYBER.2018.8688076.

[40] Z. Lai, X. Zhang, and G. Yin, "Research on key technology of multifunctional elderly-assistant & walking-assistant robot," in *Proc. 13th Int. Conf. Ubiquitous Robots Ambient Intell. (URAI)*, Aug. 2016, pp. 767–771, doi: 10.1109/URAI.2016.7733978.

[41] Z.-F. Lai, X.-D. Zhang, G. Yin, and Q. Zhang, "Research on driving control technology of a multifunctional elderly-assistant & walking-assistant robot," in *Proc. Mechatronics Autom. Eng.*, Mar. 2017, pp. 189–195, doi: 10.1142/9789813208537_0024.
[42] X. Mu, X. Zhang, Z. Lai, and O. R. Osivue, "Structural characteristic analysis of multifunctional elderly-assistant and walking-assistant robot based on SolidWorks/simulation," in *Proc. 14th Int. Conf. Ubiquitous Robots Ambient Intell. (URAI)*, Jun. 2017, pp. 941–946, doi: 10.1109/URAI.2017.7992871.
[43] O. R. Osivue, X. Zhang, X. Mu, and H. K. Kadry, "PID control of elderly assistant and walking assistant robot," in *Proc. Int. Conf. Appl. Mathematics, Modeling Simul.*, 2017, pp. 419–424, doi: 10.2991/amms-17.2017.92.
[44] X. Zhang, X. Mu, H. Xu, A. B. Alhassan, and H. K. Kadry, "Vibration characteristics analysis of human–robot coupled system for walking posture of elderly-assistant robot," *IEEE Access*, vol. 9, pp. 44217–44235, 2021, doi: 10.1109/ACCESS.2021.3066397.
[45] J. P. Chrstos and D. A. Guenther, "The measurement of static rollover metrics," SAE Int., USA, Tech. Rep. 920582, 1992, doi: 10.4271/920582.
[46] A. Naveen, H. Luo, Z. Chen, and B. Li, "Predicting wheelchair stability while crossing a curb using RGB-depth vision," in *Computers Helping People With Special Needs* (Lecture Notes in Computer Science), vol. 12377. Cham, Switzerland: Springer, 2020, pp. 394–401, doi: 10.1007/978-3-030-58805-2_47.
[47] R. L. Huston and F. A. Kelly, "Another look at the static stability factor (SSF) in predicting vehicle rollover," *Int. J. Crashworthiness*, vol. 19, no. 6, pp. 567–575, Nov. 2014, doi: 10.1080/13588265.2014.919730.
[48] Y. Shen, L. Chen, X. Yang, D. Shi, and J. Yang, "Improved design of dynamic vibration absorber by using the inerter and its application in vehicle suspension," *J. Sound Vibrat.*, vol. 361, pp. 148–158, Jan. 2016, doi: 10.1016/j.jsv.2015.06.045.
[49] Y. Li, W. Sun, J. Huang, L. Zheng, and Y. Wang, "Effect of vertical and lateral coupling between tyre and road on vehicle rollover," *Vehicle Syst. Dyn.*, vol. 51, no. 8, pp. 1216–1241, Aug. 2013, doi: 10.1080/00423114.2013.791395.
[50] A. Ueckermann and B. Steinauer, "The weighted longitudinal profile: A new method to evaluate the longitudinal evenness of roads," *Road Mater. Pavement Des.*, vol. 9, no. 2, pp. 135–157, Jan. 2008, doi: 10.1080/14680629.2008.9690111.

KHALED HAMZA received the bachelor's degree from the Faculty of Engineering at Benha, Benha University, Egypt, in 2008. He is currently pursuing the Ph.D. degree with the School of Mechanical Engineering, Xi'an Jiaotong University, China. His research interests include human–machine systems and intelligent robotics.

ZHANG XIAODONG received the Ph.D. degree from Xi'an Jiaotong University, Xi'an, China, in 1996. He is a Professor and the Ph.D. Supervisor with the School of Mechanical Engineering, Xi'an Jiaotong University. Formerly, he was a Researcher with the School of Mechanical Engineering, Sungkyunkwan University, South Korea, from 2003 to 2005. His main research interests include intelligent measurement and control, biomechatronics technology, and intelligent robotics.

MU XIAOQI was born in 1988. He received the master's degree in mechanical engineering from Zhengzhou University of Light Industry, China. He is currently pursuing the Ph.D. degree with Shaanxi Key Laboratory of Intelligent Robots, School of Mechanical Engineering, Xi'an Jiaotong University, Xi'an, China. His research interests include human–machine systems and intelligent robotics.

GILBERT MASENGO received the Bachelor of Science degree in electrical power engineering from the National University of Rwanda (NUR), and the master's degree from Xi'an Jiaotong University (XJTU), China. He is a Ph.D. Researcher with the School of Mechanical Engineering, Xi'an Jiaotong University, China. He is dedicated to designing and controlling robotics for several mechanical parts for industrial and medical applications.

AHMAD BALA ALHASSAN (Member, IEEE) received the B.Eng. degree in electrical engineering from Bayero University, Kano, Nigeria, in 2011, the M.Eng. degree in mechatronics and automatic control from the University of Technology Malaysia (UTM), in 2016, and the Ph.D. degree in mechanical engineering from Xi'an Jiaotong University, China, in 2022.

He was with the Department of Mechanical Engineering, Chulalongkorn University, Thailand, as a Postdoctoral Researcher, in 2023. He is currently with the Department of Robotics and Mechatronics, Nazarbayev University, Kazakhstan. He has authored or co-authored many research articles and international conference papers on dynamic analysis and control of crane systems, inverted pendulums, rehabilitation robots, elderly-assistant robots, power transmission line inspection robots, and wind energy conversion systems. He was a keynote speaker at the Fifth International Conference on Intelligent Science and Technology (ICIST 2023), Lanzhou, China. His current research interests include modeling, simulation, and control of mechatronic systems. He has been a member of the IEEE Young Professionals, the IEEE Control Systems Society, and the IEEE Industrial Electronics Society. He has served as a Reviewer for many refereed journals, including IEEE Access, *Journal of Mechanical Science and Technology*, and *Robotics and Autonomous Systems*.